Check for updates

ADVANCED FUNCTIONAL MATERIALS
www.afm-journal.de

$Ni_{0.25}Cu_{0.5}Sn_{0.25}$ Nanometallic Glasses As Highly Efficient Catalyst for Electrochemical Nitrate Reduction to Ammonia

Yang Liu, Shenglong Huang, Jiajia Lu, Shuyu Niu, Pei Kang Shen, Zhuofeng Hu, Panagiotis Tsiakaras,* and Shuyan Gao**

Electrochemical nitrate reduction to ammonia (NRA) is a promising approach for alleviating energy crisis and water pollution. Current NRA catalysts are challenged to simultaneously improve the rate of the adsorption and desorption processes to further increase the total activity due to the Brønsted–Evans–Polanyi (BEP) relationships. Herein, a two-step Joule heating method is utilized for the preparation of $Ni_{0.25}Cu_{0.5}Sn_{0.25}$ nanometallic glass containing synergistic catalytic sites to simultaneously enhance the adsorption and desorption processes. Kelvin probe force microscopy reveals a pronounced oscillatory behavior in the surface potential of $Ni_{0.25}Cu_{0.5}Sn_{0.25}$ nanometallic glass, which is an important feature of the synergistic catalytic site, and an empirical formula is proposed to quantitatively characterize its oscillatory characteristic. In situ electrochemical Raman spectroscopy indicates the promotion of nickel and tin atoms for nitrate adsorption and ammonia desorption processes, respectively. DFT calculations demonstrated that $Ni_{0.25}Cu_{0.5}Sn_{0.25}$ presents a wide range of adsorption energy distributions to favor the multisite synergistic catalysis. The present work provides new ideas for the design and understanding of highly active NRA catalysts.

1. Introduction

Compared with the Haber process that requires high temperature (400–500°C) and pressure (15–25 MPa) conditions,[1] electrochemical nitrate (NO_3^-) reduction to ammonia (NRA) allows convenient ammonia (NH_3) production under ambient conditions with high selectivity and reaction rate,[2,3] and is expected to be an important part of the NH_3 production pathway in the future NH_3 economy.[4,5] Among all the monometal, metallic copper (Cu) is the best known NRA catalyst, especially the Cu (111) plane exhibits an extremely high activity.[6,7] With NO_3^- adsorbed, most of the surface of Cu(111) plane adsorbed will be easily converted to more stable cuprous oxide (Cu_2O) with a small lattice structure change.[8] Thus, focusing on the design of component and structures of Cu-based catalysts to go for the improvement of the NRA reaction rate is one of the most promising directions.[9–11]

Koper et al. found that the Tafel slope of the NRA reaction is close to or higher than 120 mV dec^{-1} for most transition metals (Pt, Ir, Ru, Rh, Ag, Cu, etc.),[8] indicating that the NO_3^- to nitrite (NO_2^-) process is involved in the rate-determining step.[8,12] Copper-based materials have been widely studied for their high activity, and NRA activity can be further enhanced by doping with metals Ni or Co that have moderate adsorption capacity for protons.[13,14] According to the Arrhenius equation and the Brønsted–Evans–Polanyi (BEP) relationships,[15,16] increasing the adsorption energy of the catalytic site for NO_3^- can decrease the reaction energy barrier, which can enhance the reaction rate from NO_3^- to NO_2^-.[17] The incorporation of metals such as nickel (Ni),[13,18] cobalt (Co),[19,20] iron (Fe),[15] and other elements with higher d-band centers into Cu has been demonstrated to elevate the Fermi energy of copper, thereby elevating the

Y. Liu, S. Huang, S. Niu, S. Gao
School of Materials Science and Engineering
Henan Normal University
Xinxiang, Henan 453007, P. R. China
E-mail: shuyangao@htu.edu.cn

J. Lu
Henan Provincial Key Laboratory of Nanocomposites and Applications
Institute of Nano-Structured Functional Materials
Huanghe Science and Technology College
Zhengzhou 450006, China

The ORCID identification number(s) for the author(s) of this article can be found under https://doi.org/10.1002/adfm.202411325

[Correction added on October 7, 2024, after first online publication: Author affiliations have been updated in this version.]

DOI: 10.1002/adfm.202411325

P. K. Shen
Collaborative Innovation Center of Sustainable Energy Materials
Guangxi Key Laboratory of Electrochemical Energy Materials
Guangxi University
Nanning 530004, P. R. China

Z. Hu
School of Environmental Science and Engineering
Sun Yat-sen University
Guangzhou 510006, P. R. China
E-mail: huzhf8@mail.sysu.edu.cn

P. Tsiakaras
Laboratory of Alternative Energy Conversion Systems
Department of Mechanical Engineering
School of Engineering
University of Thessaly
Pedion Areos 38834, Greece
E-mail: tsiak@uth.gr

 © 2024 Wiley-VCH GmbH

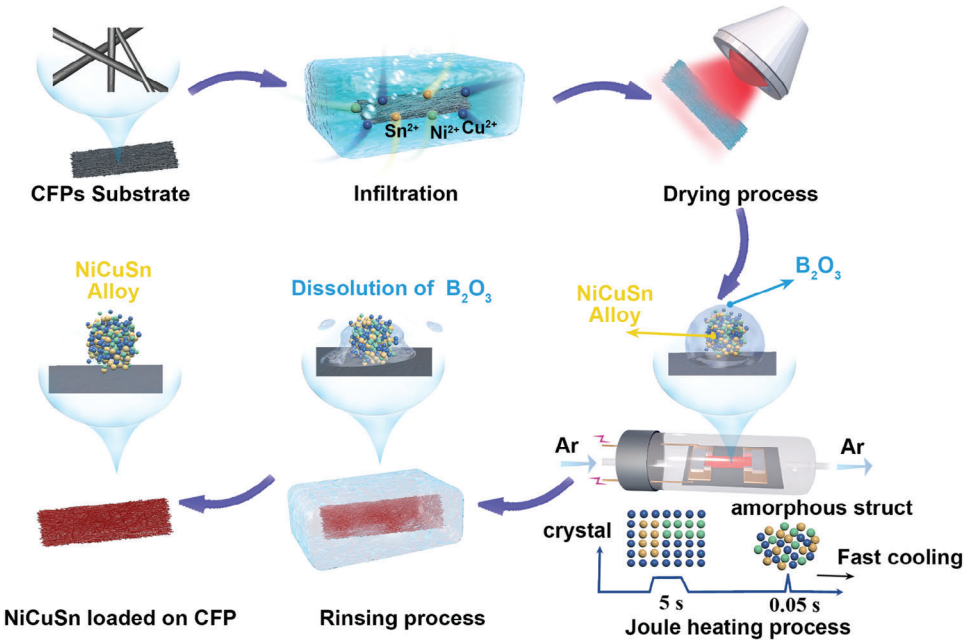

Scheme 1. Synthesis procedure for $Ni_xCu_ySn_z$-CFP by Joule thermal method.

adsorption energy. This phenomenon results in an increased population of electrons occupying the antibonding orbitals of the adsorbed NO_3^- species, which reduces the stability of N-O bonding in NO_3^-, leading to a significant improvement of onset potential and limiting current density. The thermally enhanced strategy can further increase the generation of atomic hydrogen in a tandem catalytic pathway and overcome thermodynamic barriers to facilitate NO_x conversion.[21] As the adsorption energy increases, the NH_3 desorption becomes a new rate-determining step due to the opposing adsorption energy requirements of NO_3^- and NH_3.[22,23] Therefore, it is difficult to optimize the overall process simultaneously by simply adjusting the adsorption energy in one direction. Relative to crystalline alloys, amorphous metallic glasses with long-range disordered and short-range ordered atomic arrangements have low density, abundant low-coordination sites, high density of active sites, a wide range of elemental components, and good corrosion resistance,[24] thus it is a promising way to construct synergistic catalytic sites that can simultaneously regulate multiple elementary steps through the structural advantages of metallic glasses.[25,26]

In this work, amorphous $Ni_{0.25}Cu_{0.5}Sn_{0.25}$ nanometallic glass was successfully synthesized by a new two-step Joule heating method. The Ni with strong adsorption energy and the Sn with weak adsorption energy were added on both sides of the Cu with medium adsorption energy to extend the adsorption energy distribution, taking advantage of the strong inclusiveness of metallic glass to regulate the adsorption of NO_3^- and the desorption of NH_3 simultaneously. We propose a new empirical formula that can quantitatively describe the oscillatory property of surface potential detected by the Kelvin probe force microscopy (KPFM) measurements, which can be an important indication for experimentally evaluating the synergistic catalytic site. In situ electrochemical Raman spectroscopy and theoretical calculations further revealed the synergistic catalysis on amorphous $Ni_{0.25}Cu_{0.5}Sn_{0.25}$ nanometallic glass. This work provides new ideas and methods for the synthesis and analysis of highly active nanometallic glass catalysts.

2. Results and Discussion

2.1. Synthesis and Structural Characterization

The synthesis procedure of NiCuSn-CFP nanometallic glass is illustrated in **Scheme 1**. A carbon fiber paper (CFP) was soaked in the precursor solution containing Ni^{2+}, Cu^{2+}, Sn^{2+}, and boric acid, after a dry process with an infrared baking lamp, the sample was subjected to a new two-step Joule heating methods consisting of slow (5 s, 160 K s^{-1}) and fast (0.05 s, 16000 K s^{-1}) heating process in the H_2/Ar (5% H_2) atmosphere. The B_2O_3 decomposed from boric acid above 150 °C can eliminate the non-uniform nucleation in the alloy to promote the formation of an amorphous state.[27] From our previous experiments, we found that using only the rapid heating process would lead to a large loss of metal precursors. This is due to the fact that the metal precursors would release a large amount of gas during the rapid heating process, and the ejected gas (H2O, CO, CO2, etc.) would impact the unreacted metal precursors and strip them, thus resulting in a decrease in catalyst loading. The optimized two-step Joule heating method utilizes the respective advantages of the slow and fast heating processes, respectively. The slow heating process can inhibit the metal precursor from being stripped by ejected gas and promote the full reduction of metal ions to increase the metal loading. The fast heating process is necessary to reach the melting point of the alloy in a short time, which can facilitate the trapping of heat in the sample and the rapid dissipation of heat during subsequent power-downs, thus increasing the cooling rate and promoting the formation of an amorphous structure.

© 2024 Wiley-VCH GmbH

16163028, 0, Downloaded from https://onlinelibrary.wiley.com/doi/10.1002/adfm.202411325 by Shanxi University, Wiley Online Library on [07/10/2024]. See the Terms and Conditions (https://onlinelibrary.wiley.com/terms-and-conditions) on Wiley Online Library for rules of use; OA articles are governed by the applicable Creative Commons License

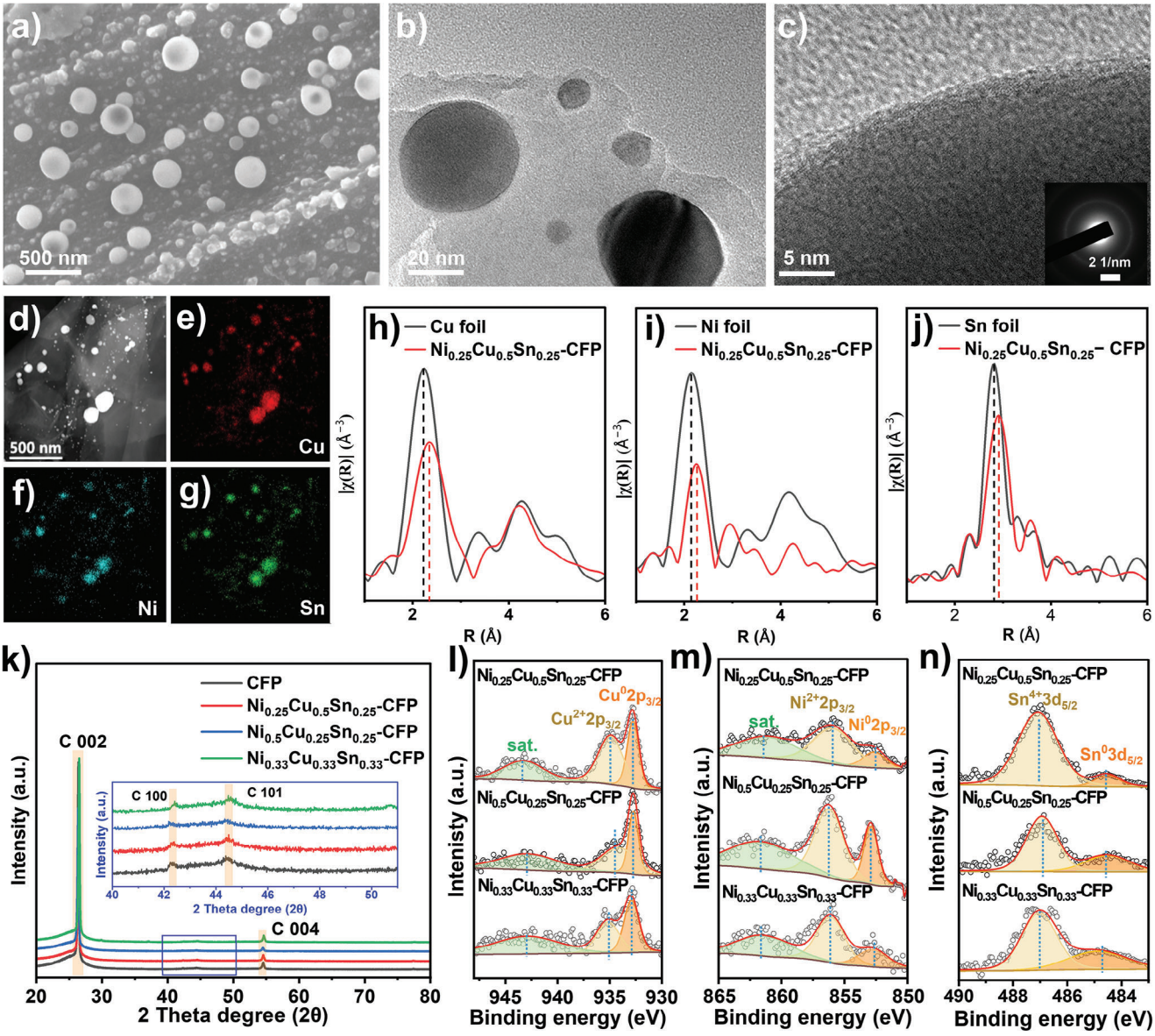

Figure 1. a) SEM and b,c) TEM images; d–g) EDS element mapping images of $Ni_{0.25}Cu_{0.5}Sn_{0.25}$-CFP; h) Cu K-edge, i) Ni K-edge and j) Sn K-edge FT-EXAFS spectra of $Ni_{0.25}Cu_{0.5}Sn_{0.25}$-CFP and corresponding metal reference; k) The XRD pattern of $Ni_xCu_ySn_z$-CFP; l) Cu 2p, m) Ni 2p and n) Sn 3d XPS spectra of $Ni_xCu_ySn_z$-CFP.

The SEM (**Figures** 1a and S1, Supporting Information) and TEM (Figure 1b,c; Figure S2, Supporting Information) images of synthesized $Ni_{0.25}Cu_{0.5}Sn_{0.25}$-CFP, $Ni_{0.5}Cu_{0.25}Sn_{0.25}$-CFP and $Ni_{0.33}Cu_{0.33}Sn_{0.33}$-CFP demonstrate a spherical morphology highly dispersed on the CFP, which can be ascribed to the full reduction of the metal precursor during the Joule heating treatment. There are no observed lattice fringes of the metals in the high-resolution TEM images, the representative broad halo rings in the selected area electron diffraction images (SAED) inserted in high-resolution TEM confirm their amorphous structure of metallic glass,[28,29] facilitating the homogeneous mixing of different elements verified by the EDS elemental mapping images (Figure 1d–g). The content of metals in each sample was detected by an inductively coupled plasma source mass spectrometer (ICP-MS), and the results showed that the proportions of each element were almost the same as the set value, and the total molar metal amount was around 9 μmol (Table S1, Supporting Information).

The normalized X-ray absorption near-edge structure (XANES) spectra of $Ni_{0.25}Cu_{0.5}Sn_{0.25}$-CFP at the Ni K-edge, Cu K-edge, and Sn K-edge are presented in Figure S3, Supporting Information, their absorption edges essentially coincide with the corresponding Cu, Ni, and Sn foils, demonstrating the predominance of the metallic state in the $Ni_{0.25}Cu_{0.5}Sn_{0.25}$-CFP. The Fourier-transformed extended X-ray absorption fine structure (FT-EXAFS) spectrum of $Ni_{0.25}Cu_{0.5}Sn_{0.25}$-CFP is shown in Figure 1h–j. The intensity of the metal peaks in $Ni_{0.25}Cu_{0.5}Sn_{0.25}$-CFP are lower and are positively shifted compared to the

© 2024 Wiley-VCH GmbH

16163028, 0, Downloaded from https://onlinelibrary.wiley.com/doi/10.1002/adfm.202411325 by Shanxi University, Wiley Online Library on [07/10/2024]. See the Terms and Conditions (https://onlinelibrary.wiley.com/terms-and-conditions) on Wiley Online Library for rules of use; OA articles are governed by the applicable Creative Commons License

standard metal samples, indicating that the coordination number decreases, and the metallic bond lengths increase. Benefiting from the unique structural features of short-range ordered and long-range disordered structures of metallic glasses,[30] it has a smaller density and larger volume relative to crystalline metals for the same atomic number and therefore has longer metallic bonds.[27] The smaller coordination number contributes to the generation of more dangling bonds on the surface with more active site centers.[31]

The XRD patterns in Figure 1k further evidence the amorphous structure of the $Ni_xCu_ySn_z$-CFP because there are no diffraction peaks of metal except for the graphite (002), (004), (100), and (101) planes, which are highly consistent with the amorphous structure characteristics.[32,33] The high-resolution XPS (HR-XPS) of Cu2p, Ni2p, and Sn3d core levels of $Ni_xCu_ySn_z$-CFP are shown in Figure 1l–n), which are deconvoluted to several peaks in Table S1 (Supporting Information) corresponding to zero valence state and oxidation state. The oxidized state of the species signal may come from surface oxidation in air, whereas it can be rapidly reduced in an actual electroreduction reaction.[34,35]

The surface structure and surface potential distribution of the metallic glass were analyzed by AFM and KPFM with atomic-level resolution (**Figure 2**a). As shown in Figure 2b, surface potential, work function, and adsorption energy are closely related,[36] the more negative the surface potential the lower its work function, and the easier it is to give electrons, thus having a strong adsorption energy for the adsorbed species in NRA. It is readily conceivable that there is an important correlation between the variation characteristic of the surface potentials and the synergistic catalytic effect. Therefore, quantitatively describing the oscillatory characteristics of the surface potential is essential to further reveal the reactivity. We start with a simple curve (Figure 2c) and gradually increase the frequency (Figure 2d) and amplitude (Figure 2e). We then construct curves with different amplitudes (Figure 2f), different frequencies (Figure 2g), and both varying amplitudes and frequencies (Figure 2h) to analyze and summarize the oscillatory characteristics.

Finally, we proposed an empirical formula to quantitatively characterize the variation of the surface potentials: $Os. = \sum_{k=0}^{n} |y_k - y_{k+1}|^2 \times n\ (|y_k - y_{k+1}| > 0.1\ mV)$, where *Os.* represents the oscillativity, which contains information from extreme points and amplitudes, n is the number of extreme points, y_0 and y_{n+1} are the intersections of the curve with the y-axis at the leftmost and rightmost ends, respectively. $y_k - y_{k+1}$ $(0 < k < n)$ denotes the difference between the vertical coordinates of two neighboring extreme points. Surface potential changes within 0.1 mV were excluded to eliminate the interference of experimental errors. This formula well describes and distinguishes the oscillatory characteristics of the above curves (Figure 2c–h), which provides experimentally new promising indicators for describing synergistic catalysis through the oscillativity of the local surface potential for multi-electron and multi-step reactions such as NRA, oxygen reduction, carbon dioxide reduction, etc.

AFM images (**Figure 3**a–d) show spherical nanoparticles of Cu-CFP, Ni-CFP, Sn-CFP, $Ni_{0.25}Cu_{0.5}Sn_{0.25}$-CFP conforming to the SEM images, and the corresponding KPFM images and 3D reconstructed pictures are respectively shown in Figure 3e–h and Figure S5 (Supporting Information). The surface potential of the carbon fiber was calibrated to be zero, and the potential of the metal surface was negative, attesting to its strong ability to give electrons.[9,26] We further performed an ultra-high-resolution KPFM for the white wireframe region in Figure 3e–h, with the scanning ranges of 500 and 20 nm in the x- and y-directions, corresponding to the resolutions of 1000 and 40, respectively, so that the spacing between the two nearest neighboring points is 0.5 nm. The surface potentials in the white line portion of Figure 3i–l were plotted separately as shown in Figure 3m–p. It is evident that the surface potential of $Ni_{0.25}Cu_{0.5}Sn_{0.25}$-CFP is highly oscillatory with a maximum value (56.88) of Os., this indicates that alloys containing metals with different work functions (Ni: 5.15 eV, Cu: 4.65 eV, Sn: 4.42 eV) can induce large surface potential oscillativity at the surface, which can facilitate the construction of synergistic catalytic sites with different adsorption energies, thus satisfying the different demands for adsorption energies of the individual elementary steps in NRA.[38]

2.2. Electrochemical NRA Performance

The IR-corrected LSV curves of different samples performed in 0.5 M Na_2SO_4 + 0.1M KNO_3 and 0.5 M Na_2SO_4 solution are presented in **Figures** 4a and S6 (Supporting Information). It is evident that the $Ni_{0.25}Cu_{0.5}Sn_{0.25}$-CFP exhibits the highest current density (−88.26 mA cm^{-2}) and onset potential (0.02 V vs. RHE at 20 mA cm^{-2}) in Figure 4b. Differences in current density (Δj) of each sample at −0.2 V vs. RHE in Na_2SO_4 and Na_2SO_4 + KNO_3 solutions are shown in Figure 4c, $Ni_{0.25}Cu_{0.5}Sn_{0.25}$-CFP demonstrates the maximum Δj (82.73 mA cm^{-2}), while Ni-CFP has the lowest Δj (10.88 mA cm^{-2}). With the negative shift of potential, the corresponding current densities of the individual samples gradually increase, and a reduction peak current appears at around −0.2 V vs. RHE for Cu-CFP, $Cu_{0.5}Ni_{0.5}$-CFP, $Ni_xCu_ySn_z$-CFP. The LSV curves of $Ni_{0.25}Cu_{0.5}Sn_{0.25}$-CFP samples at different scan rates in 0.5 M Na_2SO_4 + 0.1M KNO_3 solution are shown in Figure S7a (Supporting Information), where the reduction peak current exhibits a good linear relationship with the square root of the scan rate (Figure S7b, Supporting Information), which is consistent with that described by Randles-Sevick (R-S) equation, implying that reduction peak current is caused by the restricted mass-transfer process.

Blank experiments demonstrated that the limiting current density of CFP derives mainly from the conversion of nitrate (Figure S8, Supporting Information), and after replacing nitrate with the same concentration of nitrite, the limiting current density is reduced to $\frac{3}{4}$ of the original, attributed to the 6-electron reduction process of nitrite compared to the 8-electron process of NRA. The $Ni_{0.25}Cu_{0.5}Sn_{0.25}$-CFP has the smallest Tafel slope (Figure 4d) of 137.96 mV dec^{-1} demonstrating the fastest kinetic reaction process among all the samples. The EIS spectra (Figure 4e) were measured to analyze the reaction kinetics for the $Ni_xCu_ySn_z$-CFP, the $Ni_{0.25}Cu_{0.5}Sn_{0.25}$-CFP has the smallest diameter of semicircle (≈7.2 Ω), indicating the lowest charge transfer resistance and the fastest kinetics for NRA.

The yield rate and FE of NH_3 and NO_2^- over Cu-CFP, Ni-CFP, Sn-CFP, $Cu_{0.5}Ni_{0.5}$-CFP, $Ni_{0.25}Cu_{0.5}Sn_{0.25}$-CFP, $Ni_{0.5}Cu_{0.25}Sn_{0.25}$-

© 2024 Wiley-VCH GmbH

16163028, 0, Downloaded from https://onlinelibrary.wiley.com/doi/10.1002/adfm.202411325 by Shanxi University, Wiley Online Library on [07/10/2024]. See the Terms and Conditions (https://onlinelibrary.wiley.com/terms-and-conditions) on Wiley Online Library for rules of use; OA articles are governed by the applicable Creative Commons License

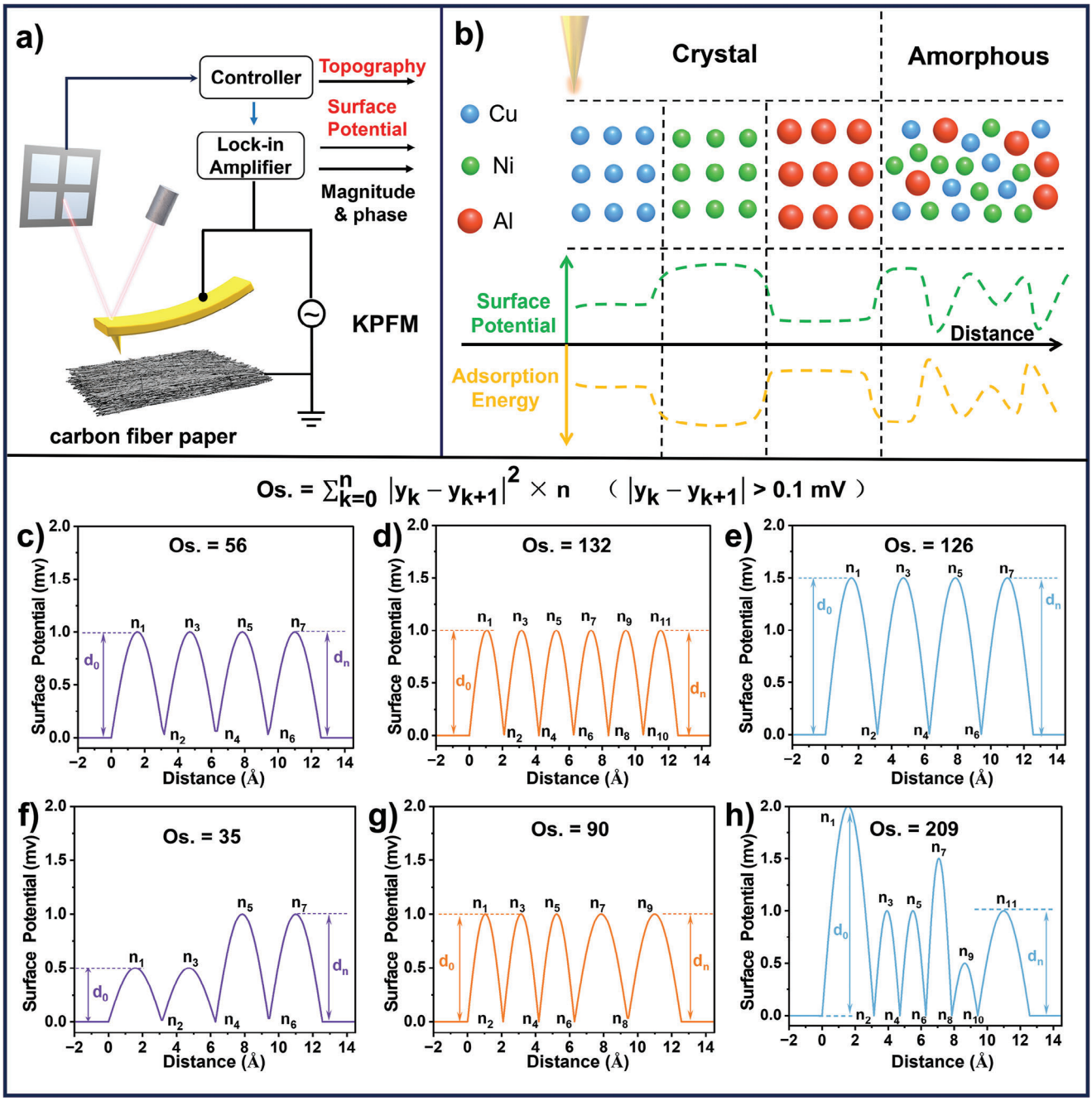

Figure 2. Schematic illustrations: a) of the KPFM and b) of surface potential and adsorption energy for crystal and amorphous. c–h) Typical curves with different oscillation characteristics and their corresponding Os. Values.

CFP, $Ni_{0.33}Cu_{0.33}Sn_{0.33}$-CFP at different potentials were investigated in Ar-saturated 0.1 mol L^{-1} KNO_3 + 0.5 mol L^{-1} Na_2SO_4 solution (Figures S9–S11, Supporting Information), the corresponding CA and absorbances curves are shown in Figures S12–S15 (Supporting Information). The results show that the NH_3 yield rate of each sample gradually increases with the decrease of potential, while the NO_2^- yield rate and FE_{NO-2} of each sample decrease with the reduction of potential. The $Ni_{0.25}Cu_{0.5}Sn_{0.25}$-CFP demonstrates the highest NH_3 yield rate of 213.86 μmol h^{-1} cm^{-2} (312.43 mmol $g_{cat.}^{-1}$ h^{-1}) and the FE_{NH3} of 98.42% at −0.2 V vs. RHE (Figure 4f,g), which is remarkable compared to recent literature at a low potential (Figure 4j, Table S4, Supporting Information).[39–42] The electrochemical active surface area (ECSA) of each sample was obtained by CV with different scan rates to further compare the respective activity (Figures S16–S18, Supporting Information), the results show that the ECSA of each sample was essentially the same (≈700 cm^2), and the ECSA-normalised NH_3 yield rate (Figure S20, Supporting Information), LSV (Figure S21a, Supporting Information) and Δj (Figure S21b, Supporting Information) still indicate

© 2024 Wiley-VCH GmbH

16163028, 0, Downloaded from https://onlinelibrary.wiley.com/doi/10.1002/adfm.202411325 by Shanxi University, Wiley Online Library on [07/10/2024]. See the Terms and Conditions (https://onlinelibrary.wiley.com/terms-and-conditions) on Wiley Online Library for rules of use; OA articles are governed by the applicable Creative Commons License

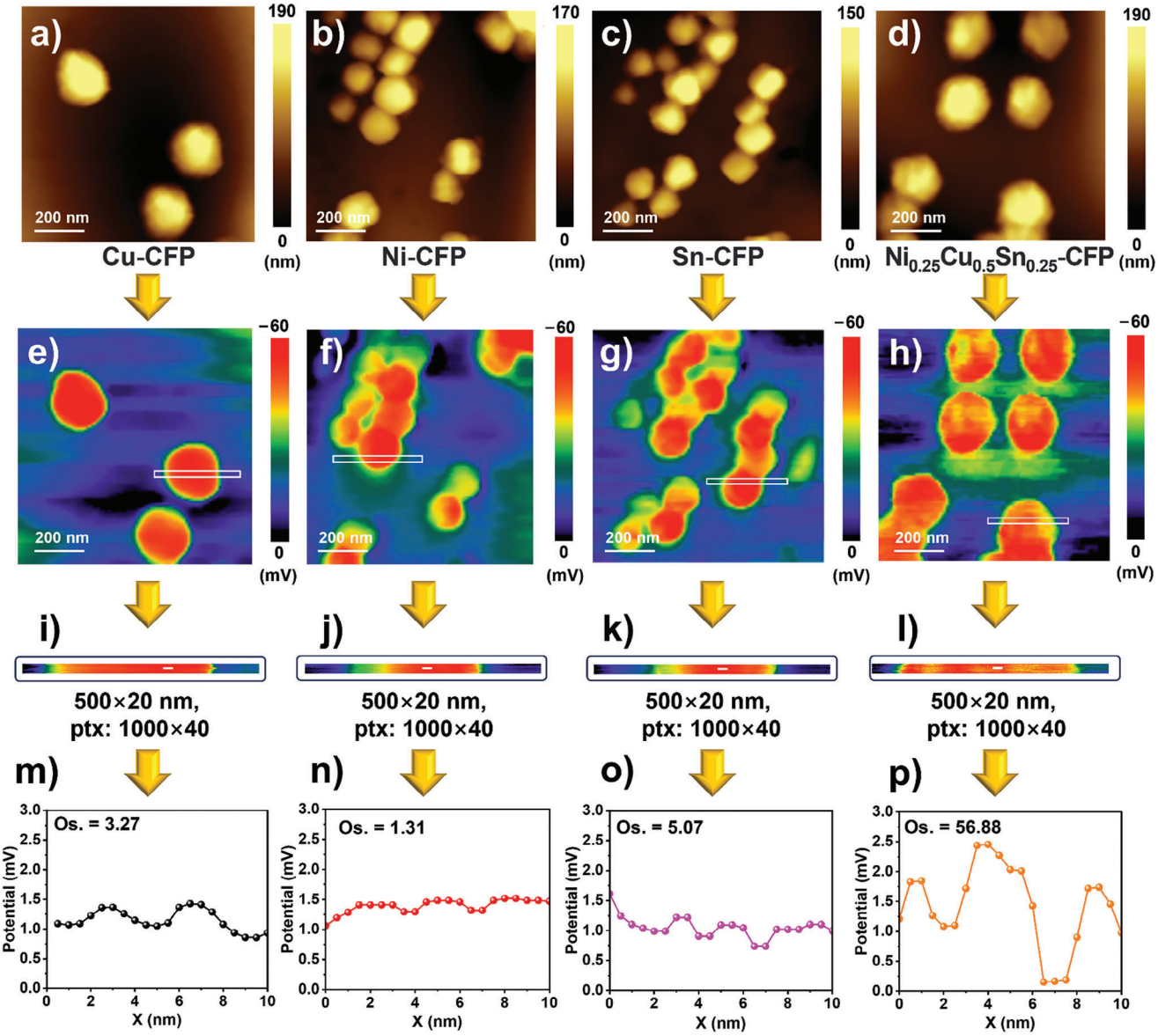

Figure 3. a–d) AFM images and (e-h) KPFM images of Cu-CFP, Ni-CFP, Sn-CFP, and $Ni_{0.25}Cu_{0.5}Sn_{0.25}$-CFP. i-l) The locally enlarged image of the selected area in Figure 2e–h and m–p) the corresponding surface potential curves of Cu-CFP, Ni-CFP, Sn-CFP, and $Ni_{0.25}Cu_{0.5}Sn_{0.25}$-CFP.

that the $Ni_{0.25}Cu_{0.5}Sn_{0.25}$-CFP has the highest NRA activity, which can be attributed to the synergistic catalytic effect between Ni, Sn and Cu.

The total FE ($FE_{NH3} + FE_{NO-2}$) of the $Ni_{0.25}Cu_{0.5}Sn_{0.25}$-CFP at 0.0, −0.1 and −0.2 V (vs. RHE) were 99.85%, 99.87% and 99.89% respectively. Whereas the total FE ($FE_{NH3} + FE_{NO-2}$) at −0.3 V was 81.53%, the gas chromatography was used to detect the possible production of H_2 and N_2 over $Ni_{0.25}Cu_{0.25}Sn_{0.25}$-CFP (Figure S19, Supporting Information), there was no N_2 signal was detected in the range of 0 to −0.3 V (vs. RHE), and only a H_2 signal was detected at −0.3V (vs. RHE), based on the comparison of peak area produced with the standard gas, the H_2 yield rate was 9.25 μmol h^{-1} cm^{-2} and the Faraday efficiency was 18.31% (Figure 4g). Both higher and lower potential conditions result in lower NH_3 yield rate and FE, which is an intriguing phenomenon attributed to the production of H_2 in the case of higher potentials and the inadequacy of atomic H and higher reactive energy barrier at lower potentials.

The NH_3 yield rate of $Ni_{0.25}Cu_{0.5}Sn_{0.25}$-CFP is almost negligible when it is performed in 0.5 mol L^{-1} Na_2SO_4 solution without KNO_3 at −0.2 V vs. RHE (Figure S22, Supporting Information), demonstrating the reliability of its NRA activity. The ^{15}N isotope labeling experiments were performed using 0.1 mol L^{-1} $K^{15}NO_3$ as the nitrogen source to further verify the reliability of NRA activity, the obtained ^1H NMR spectra are shown in Figure 4h demonstrating double peaks with a coupling constant of 72 Hz,[43,44] which is different for the three peaks with a coupling constant of 52 Hz from $K^{14}NO_3$ solution.[45] According to the standard curve (Figure S25, Supporting Information) of ^1H NMR spectra, the NH_3 yield rate (195.67 μmol h^{-1} cm^{-2}) and FE

© 2024 Wiley-VCH GmbH

16163028, 0, Downloaded from https://onlinelibrary.wiley.com/doi/10.1002/adfm.202411325 by Shanxi University, Wiley Online Library on [07/10/2024]. See the Terms and Conditions (https://onlinelibrary.wiley.com/terms-and-conditions) on Wiley Online Library for rules of use; OA articles are governed by the applicable Creative Commons License

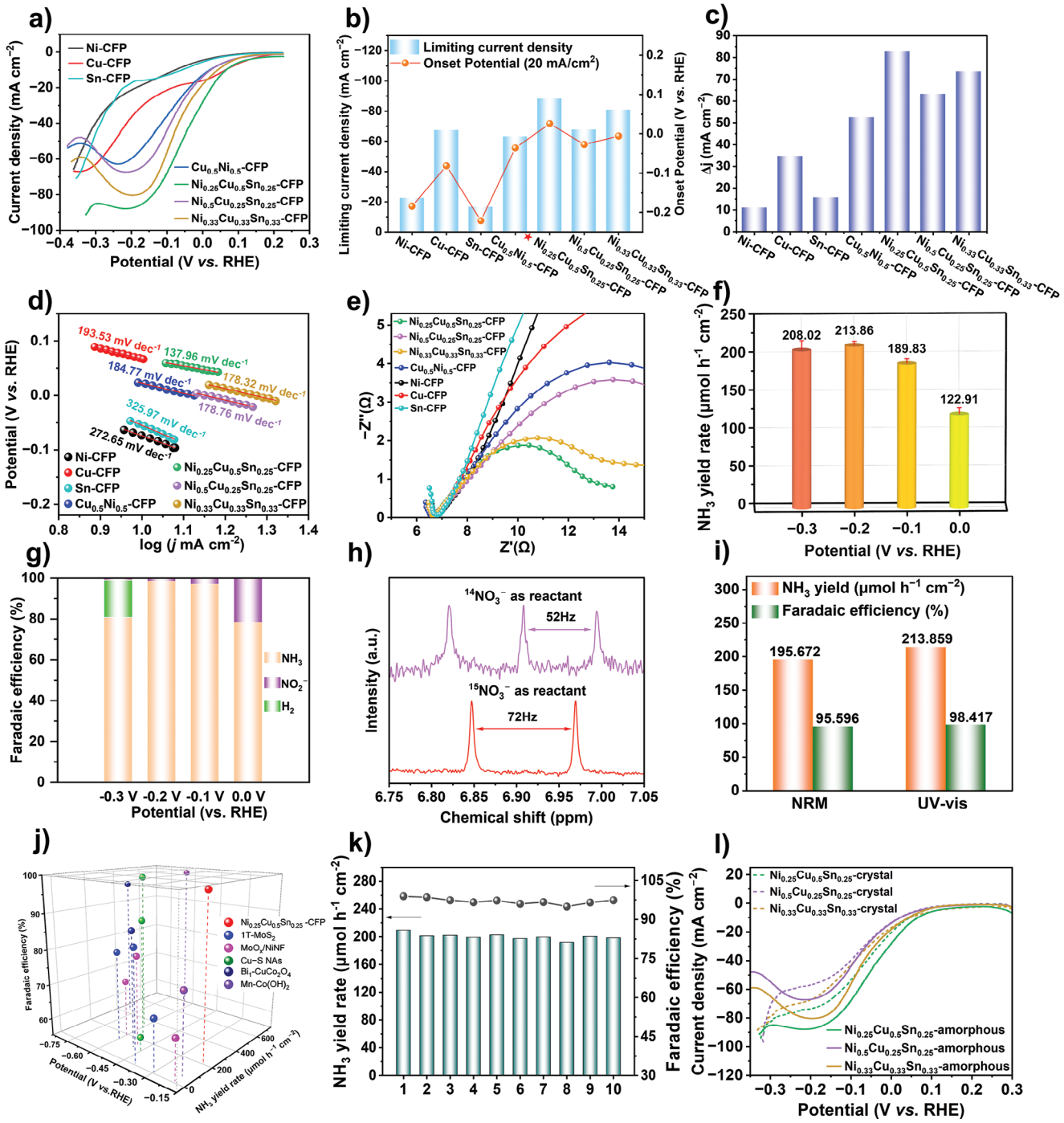

Figure 4. a) The IR-corrected LSV curves, b) comparison of onset potential and limiting current density, d) Tafel slopes, and e) EIS spectra among various samples. c) Differences in current density (Δj) of each sample at −0.2 V in Na_2SO_4 and Na_2SO_4 + KNO_3 solutions. f) NH_3 yield rate and g) Faradaic efficiency of the products of $Ni_{0.25}Cu_{0.5}Sn_{0.25}$-CFP at different potentials. h) ^1H NMR spectra of the electrolyte and k) durability test performed by $Ni_{0.25}Cu_{0.5}Sn_{0.25}$-CFP. i) NH_3 yield rate comparison of different detection methods. j) Performance comparison of $Ni_{0.25}Cu_{0.5}Sn_{0.25}$-CFP and recently reported electrocatalysts. l) The IR-corrected LSV curves between crystalline and amorphous $Ni_xCu_ySn_z$-CFP.

(95.60%) of $Ni_{0.25}Cu_{0.5}Sn_{0.25}$-CFP performed in $K^{15}NO_3$ solution demonstrate a notable congruence with the results gained from the UV–vis spectrophotometry (Figure 4i), the above results fully demonstrate the reliability and reproducibility of NAR activity of $Ni_{0.25}Cu_{0.5}Sn_{0.25}$-CFP.

The cyclic stability tests (Figure S26, Supporting Information) demonstrate that the NH_3 yield rate and FE remain above 95% after 10 cycles (Figure 4k) at −0.2 V vs. RHE. As the reaction continues, the cathode cell accumulates OH^- ions since H^+ ions are consumed for NRA, the pH change before and after the LSV

© 2024 Wiley-VCH GmbH

16163028, 0, Downloaded from https://onlinelibrary.wiley.com/doi/10.1002/adfm.202411325 by Shanxi University, Wiley Online Library on [07/10/2024]. See the Terms and Conditions (https://onlinelibrary.wiley.com/terms-and-conditions) on Wiley Online Library for rules of use; OA articles are governed by the applicable Creative Commons License

test was ≤ 0.14 (Table S2, Supporting Information), according to the Nernst equation, the change in electrode potential was ≤ 0.008 V. The pH variations of $Ni_{0.25}Cu_{0.5}Sn_{0.25}$-CFP during the CA test are shown in Figure S27 (Supporting Information), the high-activity sample will produce a higher pH value at the same time and its activity will be slightly lower, due to the decrease in the H^+ ion concentration which is unavoidable, the activity order of the samples in this work is invariable due to its small pH variation. Crystalline $Ni_xCu_ySn_z$ alloys obtained by using only the slow heating process confirmed by XRD spectra (Figure S4, Supporting Information) show a lower current density, FE, and NH_3 yield rate at the same potentials compared to that of amorphous ones (Figure 4l, Figure S28, Supporting Information), which can be attributed to the high density of active sites on the surface of the amorphous alloys.

2.3. In situ Electrochemical Raman Spectroscopy

In situ electrochemical Raman spectroscopy was employed to gain a deeper understanding of the NRA process over Cu-CFP, $Cu_{0.5}Ni_{0.5}$-CFP, and $Ni_{0.25}Cu_{0.5}Sn_{0.25}$-CFP and for comparative analysis. The potential that has a significant effect on reaction activity and reaction pathway was taken from the open circuit potential (OCP) to –0.45 V vs. RHE (**Figure 5a–c**).

The characteristic peaks of unadsorbed NO_3^-, NO_2^- and NH_3, adsorbed NO_2^- and NO_3^- involved in the NRA process are summarized in Table S5 (Supporting Information),[12,15] and their respective vibrational activities are schematically illustrated in Figure 5j. The results show that Cu_2O gradually disappears from the surface of each sample as the potential shifts negatively, and the Raman peaks of Cu-N bonds, NO_2^-, adsorbed NO_3^- and NH_3 gradually appeared when the potential was below –0.05V vs. RHE.

Compared to Cu-CFP, $Cu_{0.5}Ni_{0.5}$-CFP and $Ni_{0.25}Cu_{0.5}Sn_{0.25}$-CFP exhibited a higher intensity of peak D (NO_2^- bending), peak E (adsorbed NO_3^-) and peak H (*vs* $NO_2^-{}_{ad}$ chelating) at the same potential (Figure 5d–i). According to the Arrhenius equation and the Brønsted–Evans–Polanyi (BEP) relationships, the adsorption energy is linearly related to the activation energy, and the reaction rate constant is exponentially related to the activation energy. It indicates that Ni atoms enhance the adsorption energy for NO_3^-, decrease the activation energy of NO_3^- to NO_2^- conversion, and increase the generating rate of NO_2^-.

The peak F derives from the unadsorbed NO_3^- in solution, the ratio of the peak E/F is gradually enhanced with the decrease of the potential, which can be attributed to the fact that the applied potential improves the energy of the valence shell electron of the catalyst, and makes it easier to enter into the lowest unoccupied π^* orbitals of the NO_3^- to promote its adsorption, which is conducive to NO_3^- activation and conversion, causing a decrease in the concentration of unadsorbed NO_3^- on the surface, so that the ratio of the peak E/F could be an index for determining the activity of the catalysts. The $Ni_{0.25}Cu_{0.5}Sn_{0.25}$-CFP exhibits a higher intensity of the peak G (NH wagging in NH_3) at the same potential compared to Cu-CFP and $Cu_{0.5}Ni_{0.5}$-CFP (Figure 5g–i), suggesting that the incorporation of Sn atoms further enhances the NRA activity, which can be attributed to its provision of a weaker adsorption site in favor of NH_3 desorption.

2.4. DFT Calculations

DFT calculations were used to further reveal the adsorption energy distribution of the amorphous alloy surfaces. The adsorption energies of different sites for NO_3^- were calculated on the geometrically optimized Cu(111) (**Figure 6a**), $Cu_{0.5}Ni_{0.5}$(111) (Figure 6b), and amorphous $Ni_{0.25}Cu_{0.5}Sn_{0.25}$(111) (Figure 6c) planes. It is observed that the atomic arrangement on the surface of amorphous $Ni_{0.25}Cu_{0.5}Sn_{0.25}$(111) is more disordered compared with crystalline Cu(111) and $Cu_{0.5}Ni_{0.5}$(111), which creates conditions for the generation of diverse adsorption sites.

The adsorption energies of different sites on the corresponding surfaces are shown in Figure 6d–f), the adsorption energy for NO_3^- on the pure Cu surface is mainly distributed in the range of −2.3 to −2.4 eV, and the curve is relatively flat. The adsorption energy of $Cu_{0.5}Ni_{0.5}$ surface for NO_3^- is chiefly located in the range of −2.4 to −2.9 eV, which becomes larger overall due to the addition of Ni atoms, and the curve exhibits fluctuation.

It is obvious that the amorphous $Ni_{0.25}Cu_{0.5}Sn_{0.25}$(111) plane exhibits the broadest range of adsorption energy distribution (from –2.3 eV to –3.3 eV), in which case the maxima and minima of the surface adsorption energy shift in the positive and negative directions, respectively. The adsorption energy on the surface of $Ni_{0.25}Cu_{0.5}Sn_{0.25}$(111) planes is more oscillatory compared with crystalline Cu(111) and $Cu_{0.5}Ni_{0.5}$(111), which coincides with the oscillation of the surface potential distribution measured by KPFM. The oscillatory property of the adsorption energy present in the sub-nanometer localized range can facilitate the simultaneous promotion of multiple elementary steps as well as overflow processes, thus having the potential to construct synergistic catalytic mechanisms.

The wide distribution of adsorption energy can provide more synergistic catalytic sites that are beneficial for the 8-electronic NRA process: i) stronger adsorption energy sites promote the dissociation of NO_3^-; ii) medium adsorption energy sites facilitate the rapid transfer of intermediate species (*NO_2, *NO, *NH, *NH_2, etc.); iii) weakly adsorbed sites enhance the desorption of NH_3. These synergistic catalytic sites (**Figure 7b**) hold the potential to independently regulate the reaction rate for each elemental step, offering a promising avenue for breaking the BEP relations.

3. Conclusions

In summary, the $Ni_{0.25}Cu_{0.5}Sn_{0.25}$ nanometallic glass dispersed on carbon fibers was prepared using a new two-step Joule heating method, the long-range disordered structural features of it promoted the irregular arrangement of atoms. The $Ni_{0.25}Cu_{0.5}Sn_{0.25}$ nanometallic glass exhibited a more oscillatory surface potential and a wider adsorption energy distribution, providing a robust basis for multisite synergistic effects containing strong, medium, and weak adsorption sites, achieving the outstanding NH_3 yield rate of 213.86 μmol h^{-1} cm^{-2} and FE of 98.42% at −0.2 V (vs. RHE). The present work illuminatingly provides a promising material design strategy to bypass the Brønsted–Evans–Polanyi (BEP) relationships and offers important insights for quantitatively studying multisite synergistic effects from surface potential oscillatory properties.

© 2024 Wiley-VCH GmbH

16163028, 0, Downloaded from https://onlinelibrary.wiley.com/doi/10.1002/adfm.202411325 by Shanxi University, Wiley Online Library on [07/10/2024]. See the Terms and Conditions (https://onlinelibrary.wiley.com/terms-and-conditions) on Wiley Online Library for rules of use; OA articles are governed by the applicable Creative Commons License

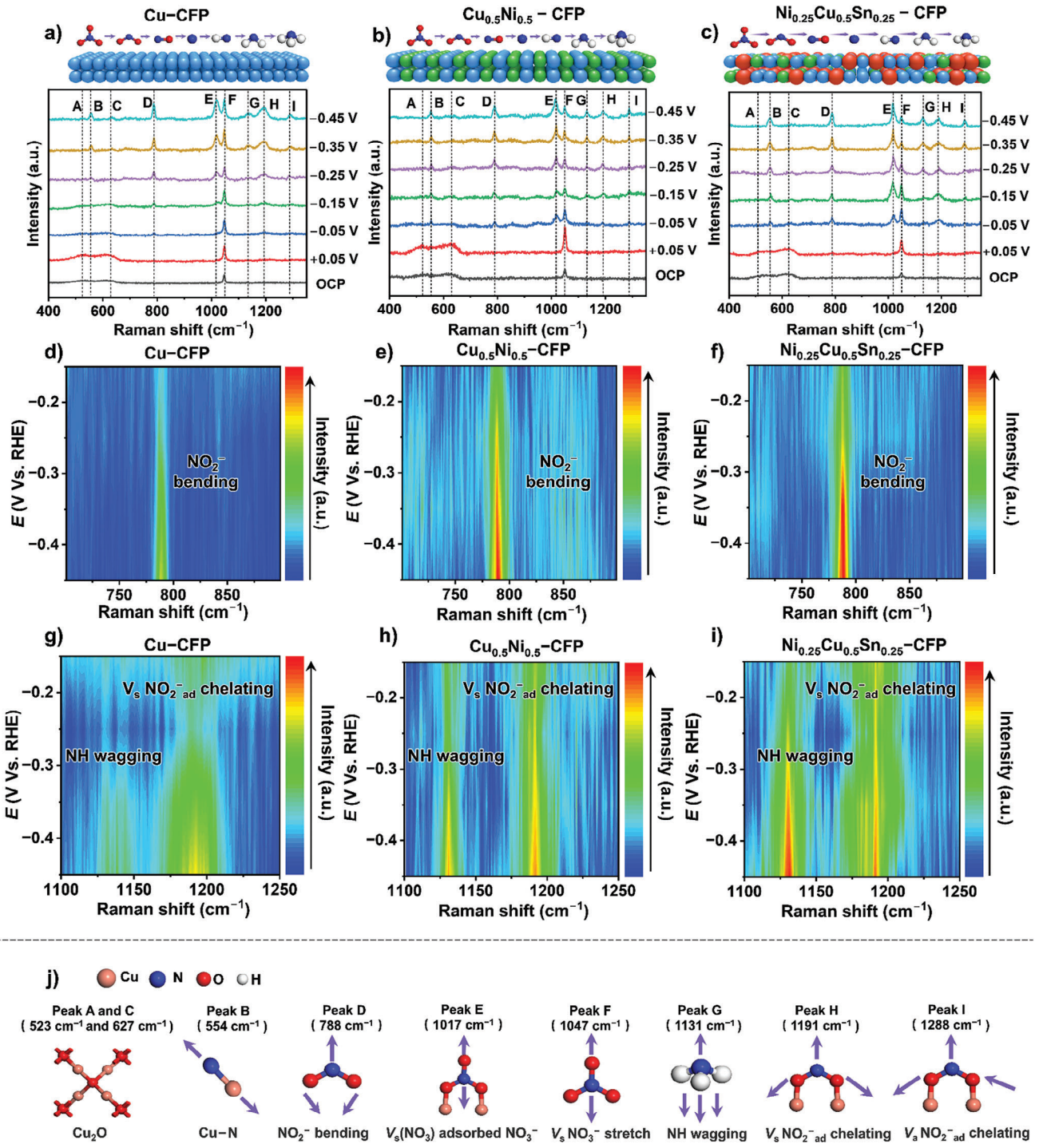

Figure 5. In situ electrochemical Raman spectra of a) Cu-CFP b) $Cu_{0.5}Ni_{0.5}$-CFP and c) $Ni_{0.25}Cu_{0.5}Sn_{0.25}$-CFP from open circuit potential (OCP) to −0.45 V. The intensity of peak D and peak G for d,g) Cu-CFP e,h) $Cu_{0.5}Ni_{0.5}$-CFP and f,i) $Ni_{0.25}Cu_{0.5}Sn_{0.25}$-CFP at different potentials. j) Schematic diagram of the vibration model of the adsorbed species and corresponding peaks.

4. Experimental Section

Chemicals and Materials: All the following reagents were analytically pure and did not require further purification treatment. Copper chloride dihydrate ($CuCl_2{\cdot}2H_2O$, 99%), nickel chloride hexahydrate ($NiCl_2{\cdot}6H_2O$, 99%), Tin (II) dichloride dihydrate ($SnCl_2{\cdot}2H_2O$, 98%), nitrate of potash (KNO_3, 99.0%), potassium nitrite (KNO_2, 97%), sodium hydroxide (NaOH, 98%), sodium sulfate (Na_2SO_4, 99%), sodium hypochlorite (NaClO, effective chlorine concentration of ≥ 5.0%), sodium salicylate ($C_7H_5O_3Na$, ≥ 99.5%), sodium nitroferricyanide(III) dihydrate

© 2024 Wiley-VCH GmbH

16163028, 0, Downloaded from https://onlinelibrary.wiley.com/doi/10.1002/adfm.202411325 by Shanxi University, Wiley Online Library on [07/10/2024]. See the Terms and Conditions (https://onlinelibrary.wiley.com/terms-and-conditions) on Wiley Online Library for rules of use; OA articles are governed by the applicable Creative Commons License

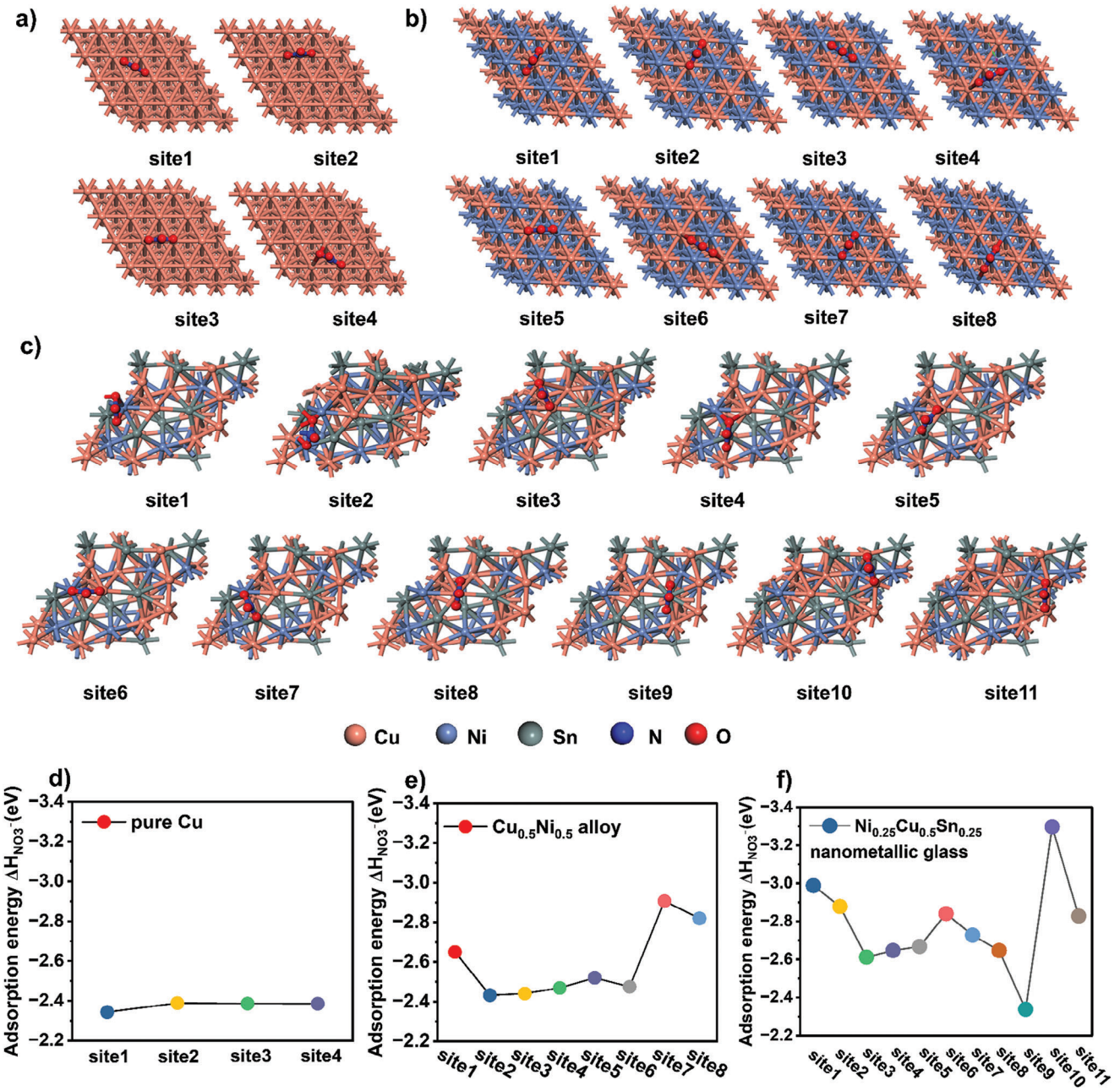

Figure 6. Nitrate adsorption models at various active sites on pure a) Cu, b) $Cu_{0.5}Ni_{0.5}$ alloy, and c) $Ni_{0.25}Cu_{0.5}Sn_{0.25}$ nanometallic glass substrates, along with the corresponding adsorption energy results for d) pure Cu, e) $Cu_{0.5}Ni_{0.5}$ alloy, and f) $Ni_{0.25}Cu_{0.5}Sn_{0.25}$ nanometallic glass.

($C_5FeN_6Na_2O\ 2H_2O$, 99%) were purchased from Aladdin Chemistry Co., Ltd. The dimethyl sulfoxide-d6 (C_2D_6SO), potassium nitrate-15N ($K^{15}NO_3$), ammonium chloride-15N ($^{15}NH_4Cl$), hydrochloric acid (HCl), sulfuric acid (H_2SO_4), and anhydrous ethanol were acquired by Shanghai Macklin Reagent Co., Ltd. The boric acid (H_3BO_4, 99.5%) was obtained from Tianjin Deen Chemical Reagent Co. Ltd. Carbon fiber paper (CFP) was obtained by Suzhou Sinero Technology Co., Ltd.

Preparation of Copper–Nickel–Tin Nanometallic Glasses: The metal precursor solution was prepared using $CuCl_2{\cdot}2H_2O$, $NiCl_2{\cdot}6H_2O$, H_3BO_4, and $SnCl_2{\cdot}2H_2O$ as solutes and ethanol as solvent, which was named $Ni_xCu_ySn_z$, where x, y and z represent the proportions of Ni, Cu and Sn in the total metal concentration of the mixed precursor solution respectively, the concentration of total metal ions and H_3BO_4 were 0.3 and 0.2 mol L^{-1}. The B_2O_3 formed by H_3BO_4 at high temperatures could effectively eliminate the generation of non-uniform nucleation and inhibit crystallization. Before immersion in the precursor solution, the prepared CFPs (2.0 cm × 0.4 cm) were calcined on an alcohol lamp to improve hydrophilicity. The impregnated CFPs, loaded with different proportions of $Ni_xCu_ySn_z$ metal precursors, were fully dried by an infrared baking lamp. The dried samples then underwent a two-step Joule heating process, comprising a slow (5.00 s, 160 K s^{-1}) and a fast (0.05 s, 16000 K s^{-1}) heating phase in an Ar atmosphere. This process resulted in the formation of a series of nanometallic glass samples denoted as $Ni_{0.25}Cu_{0.5}Sn_{0.25}$-CFP, $Ni_{0.5}Cu_{0.25}Sn_{0.25}$-CFP, and $Ni_{0.33}Cu_{0.33}Sn_{0.33}$-CFP (CFP denotes carbon fiber paper).

© 2024 Wiley-VCH GmbH

16163028, 0, Downloaded from https://onlinelibrary.wiley.com/doi/10.1002/adfm.202411325 by Shanxi University, Wiley Online Library on [07/10/2024]. See the Terms and Conditions (https://onlinelibrary.wiley.com/terms-and-conditions) on Wiley Online Library for rules of use; OA articles are governed by the applicable Creative Commons License

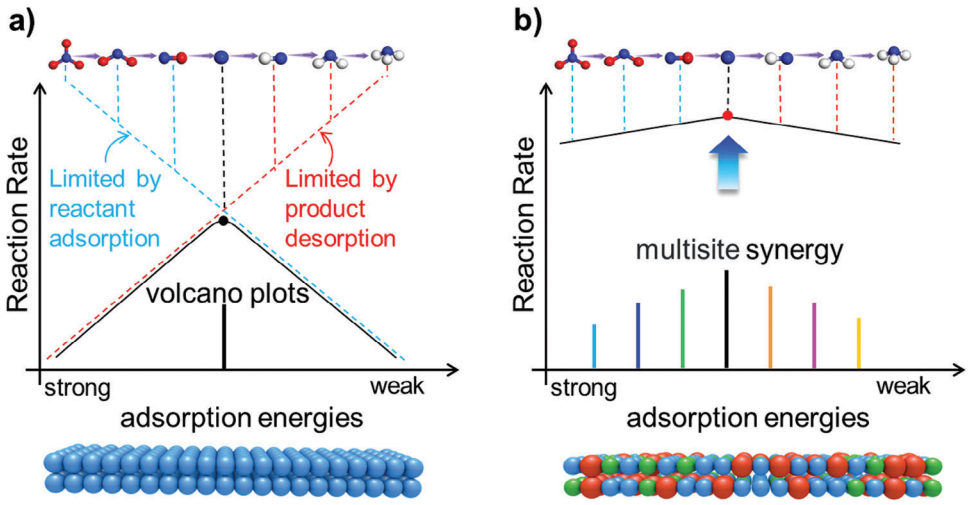

Figure 7. a) volcano plots derived from BEP relationships on the singular site, b) multisite synergy to breaking the BEP relationships on the synergistic sites.

Characterization of Materials: The morphology of the nanometallic glass loaded on CFP was obtained using high-resolution field emission scanning electron microscopy (SU8100 Hitachi). Besides, a transmission electron microscope (Jem-2100F JEOL) was carried out to obtain the transmission electron microscope (TEM) images, selected area electron diffraction (SAED) images, energy dispersive spectroscopy (EDS), and elements mapping of the catalysts. The crystal structure of the catalyst was determined by X-ray diffraction (XRD) instrument (Empyrean, Malvern Panalytic) with Cu Kα radiation. Elemental valence analysis was carried out using X-ray Photoelectron Spectroscopy (XPS) on a Thermo Scientific Escalab 250Xi X-ray photoelectron spectrometer. The C1s binding energy calibration was set at 284.8 eV to facilitate an accurate investigation of elemental valence. The UV-vis absorption spectra were conducted on a PerkinElmer LAMBDA 1050+. The nuclear magnetic resonance (NMR) measurements were performed using a Bruker 600-MHz AVANCE III HD spectrometer for ^{15}N isotope experiments. The pH of the electrolyte was measured by a pH meter (PHS-25 INESA Scientific Instrument. Co., LTD) and the gases produced during the reaction were detected by a gas chromatograph (7820 Agilent) with a thermal conductivity detector (TCD).

In situ Raman spectroscopy was detected by a HORIBA LabRAM Odyssey Nano with a liquid cell connected with an electrochemical workstation to measure the stretching vibration characteristic of intermediate species and the surface catalyst. A 10× objective was used to locate the sample on a 2D moving stage with a tungsten halogen lamp, and then a 633 nm 9 mW laser was used to illuminate the sample surface after switching to the 50× objective, which had a higher numerical aperture (0.5) that could improve the spatial resolution and collect more Raman scattering signals compared to the numerical aperture of the 10× objective (0.25). The acquisition time, number of accumulations, and confocal hole were set to 10 s, 2, and 100, respectively. Atomic force microscopy (AFM) and Kelvin probe force microscopy (KPFM) were employed to analyze the surface morphology and surface potential of the samples on an AIST-NT Smart SPM scanning probe microscope. After adjusting the optical path and finding the resonance frequency, the tip of the cantilever beam of the probe was placed directly on the carbon fiber through the 80× objective, after which the carrier stage was raised appropriately and the commands of approach and landing were subsequently executed. The scanning frequency and resonance frequency of the probe in tapping mode were 1 Hz and 130 kHz, respectively.

Electrochemical Measurements: The classical three-electrode system performed by an electrochemical workstation (DH7001, DongHua Analytical, China) was applied on an H-type cell configured with a Celgard 3501 membrane, the reversible hydrogen electrode (RHE, ALS 013373 RHEK), CFP (0.2 cm^2) loaded with catalyst and platinum foil (1.0 cm^2) serves as the reference, working and counter electrode, respectively. 40 mL of 0.5 mol L^{-1} Na_2SO_4 and 0.1 mol L^{-1} KNO_3 mixed solution was used as the electrolyte solution for each side of the H-type cell. The linear sweep voltammetry (LSV) method was carried out to study the polarization curve at a scanning rate of 5 mV/s. The ammonia yield rate and Faradaic efficiency were measured by the chronoamperometry (CA) tests within 30 min. Electrochemical impedance spectroscopy (EIS) was implemented to explore the kinetics and mass transfer processes at –0.15 V (vs. RHE) ranging from 0.1 kHz to 100 kHz.

Determination of NH_3: The concentration of ammonia in the cathode chamber after the CA test was measured by the indigo method on a UV-visible spectrophotometer. The process was as follows: Firstly, the coloring agent "A" (0.5 g NaOH and 1 mL NaClO mixed in 100 ml deionized water) and the coloring agent "B" (5 g $C_7H_5O_3Na$, 0.02 g $C_5FeN_6Na_2O$ and 0.25 g NaOH mixed in 100 mL deionized water) were prepared and placed in the refrigerator. Due to the high concentration of NH_3 in the electrolyte after the CA test, it was diluted 10 times with deionized water to make subsequent measurements of absorbance. Secondly, 0.5 mL each of coloring agents A and B were added to 2 ml of the diluted electrolyte and let stand for 1 h in a sheltered environment. The absorbance of the solution was measured by a UV-Vis spectrophotometer in the wavelength range of 750 to 550 nm. The absorbance at ≈660 nm was used to determine the NH_3 concentration using a pre-established standard curve (Figure S23, Supporting Information), which was plotted from a series of absorbance values of solutions with known NH_3 concentrations.

Determination of NO_2^-: The color agent for detecting NO_2^- was prepared with deionized water (50 mL), phosphoric acid (85 wt%, 10 mL), sulfanilamide (4 g), and N-(1-naphthyl) ethylenediamine dihydrochloride (0.2 g). A series of NO_2^- solutions (2.5 mL) with known concentrations were mixed separately with 0.1 mL of the color agent, and then placed under dark conditions for 20 minutes to test the absorbance at 540 nm using a UV-visible spectrophotometer. The obtained absorbance curves and standard curve for quantitatively detecting NO_2^- were shown in Figure S24, Supporting Information.

Calculation of the FE and NH_3 Yield Rate: The Faradaic efficiency of produced NH_3 (FE_{NH_3}) and NO_2^- ($FE_{NO_2^-}$), the yield rates of NH_3 (Y_{NH_3}) and NO_2^- ($Y_{NO_2^-}$) were calculated by the following equations:

$$FE_{NH_3} = 8 \times F \times C_{NH_3} \times V / Q \quad (1)$$

$$Y_{NH_3} = \left(C_{NH_3} \times V\right) / (t \times S) \quad (2)$$

© 2024 Wiley-VCH GmbH

16163028, 0, Downloaded from https://onlinelibrary.wiley.com/doi/10.1002/adfm.202411325 by Shanxi University, Wiley Online Library on [07/10/2024]. See the Terms and Conditions (https://onlinelibrary.wiley.com/terms-and-conditions) on Wiley Online Library for rules of use; OA articles are governed by the applicable Creative Commons License

$$FE_{NO_2^-} = 2 \times F \times C_{NO_2^-} \times V / Q \quad (3)$$

$$Y_{NO_2^-} = \left(C_{NO_2^-} \times V\right) / (t \times S) \quad (4)$$

where F was Faraday's constant (96485 C mol^{-1}), C_{NH_3} and $C_{NO_2^-}$ are the concentration of NH_3 and NO_2^-, V was the volume (40 mL) of the electrolyte in the cathode chamber, and t was the reaction duration (1800 s), while Q and S represent the total amount of electric charge and the geometric surface area (0.2 cm^2) of the electrode, respectively.

$K^{15}NO_3$ Isotope Labeling Experiments: Isotope experiments were conducted by replacing $K^{14}NO_3$ with the same concentration of $K_{15}NO_3$. After the CA test, the electrolyte (0.6 L) was added dropwise into a mixed solution, which contained 0.025 L of H_2SO_4, and 0.05 L of DMSO-d6. The ^1H NMR spectra were acquired via the NOESY method with previously reported parameters.[15] A standard curve was prepared from a known concentration (2, 4, 6, 8, 10 mmol L^{-1}) of $^{15}NH_4Cl$ solution.

Computational Simulation Details: The density functional theory (DFT) calculations were performed by the Cambridge sequential total energy package (CASTEP) with the Perdew-Burke-Ernzerhof (PBE) of generalized gradient approximation (GGA) functional. The $Cu_{0.5}Ni_{0.5}$(111) was constructed by replacing half of the Cu atoms with Ni atoms based on the Cu(111) surface. Besides, $Ni_{0.25}Cu_{0.5}Sn_{0.25}$(111) were constructed by replacing half of the Ni atoms with Sn atoms based on the $Cu_{0.5}Ni_{0.5}$(111) surface. A 3-layer (4×4) supercell with a vacuum thickness of 25 Å was configurated to all computational models. The energy cut-off was adjusted to 500 eV for relaxation, energy, and electronic property calculations. The convergence tolerance of energy was regulated to 1.0×10^{-6} eV per atom, and the maximal displacement and force were 1.0×10^{-3} Å and 0.03 eV $Å^{-1}$. The maximum number of SCF iterations was set to 400 and the rest of the parameters took on default values. The simulated amorphous $Ni_{0.25}Cu_{0.5}Sn_{0.25}$(111) was obtained by the dynamic operation under the canonical ensemble NVT until the systems reached the equilibrium state, during this process the temperature went from 298 K to 1728 K and back to 298 K. The adsorption energy was calculated by the Equation 5:[46]

$$\Delta E_{abs} = E_{M-S} - E_M - E_S \quad (5)$$

where M, S, and *abs* represent molecules, substrates, and absorption energy, respectively.

Supporting Information

Supporting Information is available from the Wiley Online Library or from the author.

Acknowledgements

This work was supported by the Special Project of Henan Provincial Key Research, Development, and Promotion (Science and Technology) (Grant No. 212102310060), the National Natural Science Foundation of China (U22A20253, 52401275), the Fellowship of China Postdoctoral Science Foundation (Grant No. 2021M701116), and LvLiang Cloud Computing Center of China (TianHe-2).

Conflict of Interest

The authors declare no conflict of interest.

Author Contributions

Y.L. conceptualized, investigated, curated data, conducted formal analysis, and wrote the original draft; S.H. investigated, curated data, and visualized results; J.L. investigated and validated; S.N. conducted formal analysis and validated; P.K.S. conceptualized and reviewed and edited the writing; Z.H. developed methodology and wrote the original draft; P.T. conceptualized, validated, and reviewed and edited the writing; S.G. conceptualized, supervised, and provided resources.

Data Availability Statement

The data that support the findings of this study are available from the corresponding author upon reasonable request.

Keywords

ammonia synthesis, amorphous alloy, multisite synergy, nanometallic glass, nitrate reduction

Received: June 27, 2024
Revised: September 10, 2024
Published online:

[1] D. Hao, Y. Liu, S. Gao, H. Arandiyan, X. Bai, Q. Kong, W. Wei, P. K. Shen, B. J. Ni, *Mater. Today* **2021**, *46*, 212.
[2] S. Han, H. Li, T. Li, F. Chen, R. Yang, Y. Yu, B. Zhang, *Nat. Catal.* **2023**, *6*, 402.
[3] A. Wu, J. Yang, B. Xu, X. Y. Wu, Y. Wang, X. Lv, Y. Ma, A. Xu, J. Zheng, Q. Tan, Y. Peng, Z. Qi, H. Qi, J. Li, Y. Wang, J. Harding, X. Tu, A. Wang, J. Yan, X. Li, *Appl Catal B* **2021**, *299*, 120667.
[4] H. Xu, Y. Ma, J. Chen, W. Zhang, J. Yang, *Chem. Soc. Rev.* **2022**, *51*, 2710.
[5] K. Dong, Y. Yao, H. Li, H. Li, S. Sun, X. He, Y. Wang, Y. Luo, D. Zheng, Q. Liu, Q. Li, D. Ma, X. Sun, B. Tang, *Nat Synth* **2024**, *3*, 763.
[6] Y. Zhang, Y. Wang, L. Han, S. Wang, T. Cui, Y. Yan, M. Xu, H. Duan, Y. Kuang, X. Sun, *Angew. Chem., Int. Ed.* **2023**, *62*, 202213711.
[7] H. Zhang, H. Wang, X. Cao, M. Chen, Y. Liu, Y. Zhou, M. Huang, L. Xia, Y. Wang, T. Li, D. Zheng, Y. Luo, S. Sun, X. Zhao, X. Sun, *Adv. Mater.* **2024**, *36*, 2312746.
[8] G. E. Dima, A. C. A. de Vooys, M. T. M. Koper, *J. Electroanal. Chem.* **2003**, *554–555*, 15.
[9] J. Liang, Z. Li, L. Zhang, X. He, Y. Luo, D. Zheng, Y. Wang, T. Li, H. Yan, B. Ying, S. Sun, Q. Liu, M. S. Hamdy, B. Tang, X. Sun, *Chem* **2023**, *9*, 1768.
[10] H. Guo, M. Li, Y. Yang, R. Luo, W. Liu, F. Zhang, C. Tang, G. Yang, Y. Zhou, *Small* **2023**, *19*, 2207743.
[11] S. Luo, H. Guo, T. Li, H. Wu, F. Zhang, C. Tang, G. Chen, G. Yang, Y. Zhou, *Appl. Catal., B* **2024**, *351*, 123967.
[12] D. P. Butcher, A. A. Gewirth, *Nano Energy* **2016**, *29*, 457.
[13] Y. Y. Lou, Q. Z. Zheng, S. Y. Zhou, J. Y. Fang, O. Akdim, X. Y. Ding, R. Oh, G. S. Park, X. Huang, S. G. Sun, *ACS Catal.* **2024**, *14*, 5098.
[14] H. Li, S. Li, R. Guan, Z. Jin, D. Xiao, Y. Guo, P. Li, *ACS Catal.* **2024**, *14*, 12042.
[15] Y. Liu, J. Ma, S. Huang, S. Niu, S. Gao, *Nano Energy* **2023**, *117*, 108840.
[16] J. Zhang, C. Guo, S. Fang, X. Zhao, L. Li, H. Jiang, Z. Liu, Z. Fan, W. Xu, J. Xiao, M. Zhong, *Nat. Commun.* **2023**, *14*, 1298.
[17] T. Li, C. Tang, H. Guo, J. Yang, F. Zhang, G. Yang, Y. Zhou, *Chem. Eng. J.* **2024**, *485*, 149560.
[18] Y. Wang, A. Xu, Z. Wang, L. Huang, J. Li, F. Li, J. Wicks, M. Luo, D. H. Nam, C. S. Tan, Y. Ding, J. Wu, Y. Lum, C. T. Dinh, D. Sinton, G. Zheng, E. H. Sargent, *J. Am. Chem. Soc.* **2020**, *142*, 5702.
[19] Y. Chen, Y. Zhao, Z. Zhao, Y. Liu, *Mater. Today Energy* **2022**, *29*, 101112.
[20] J. Y. Fang, Q. Z. Zheng, Y. Y. Lou, K. M. Zhao, S. N. Hu, G. Li, O. Akdim, X. Y. Huang, S. G. Sun, *Nat. Commun.* **2022**, *13*, 7899.

© 2024 Wiley-VCH GmbH

16163028, 0, Downloaded from https://onlinelibrary.wiley.com/doi/10.1002/adfm.202411325 by Shanxi University, Wiley Online Library on [07/10/2024]. See the Terms and Conditions (https://onlinelibrary.wiley.com/terms-and-conditions) on Wiley Online Library for rules of use; OA articles are governed by the applicable Creative Commons License

[21] K. Liu, H. Li, M. Xie, P. Wang, Z. Jin, Y. Liu, M. Zhou, P. Li, G. Yu, *J. Am. Chem. Soc.* **2024**, *146*, 7779.
[22] T. Hu, C. Wang, M. Wang, C. M. Li, C. Guo, *ACS Catal.* **2021**, *11*, 14417.
[23] J. Zhou, F. Pan, Q. Yao, Y. Zhu, H. Ma, J. Niu, J. Xie, *Appl Catal B* **2022**, *317*, 121811.
[24] Y. Yang, B. He, H. Ma, S. Yang, Z. Ren, T. Qin, F. Lu, L. Ren, Y. Zhang, T. Wang, X. Liu, L. Chen, *Acta Phys.Chim. Sin* **2022**, *38*, 2201050.
[25] Y. Zhai, X. Ren, B. Wang, S. (Frank) Liu, *Adv. Funct. Mater.* **2022**, *32*, 2207536.
[26] Q. Wu, F. Zhu, G. Wallace, X. Yao, J. Chen, *Chem. Soc. Rev.* **2024**, *53*, 557.
[27] R. Jiang, Y. Da, Z. Chen, X. Cui, X. Han, H. Ke, Y. Liu, Y. Chen, Y. Deng, W. Hu, *Adv. Energy Mater.* **2022**, *12*, 2101092.
[28] B. Sarac, Y. P. Ivanov, M. Micusik, M. Omastova, A. S. Sarac, A. I. Bazlov, V. Zadorozhnyy, A. L. Greer, J. Eckert, *ACS Catal.* **2022**, *12*, 9190.
[29] Z. Jia, K. Nomoto, Q. Wang, C. Kong, L. Sun, L. C. Zhang, S. X. Liang, J. Lu, J. J. Kruzic, *Adv. Funct. Mater.* **2021**, *31*, 2101586.
[30] H. Wang, Q. He, X. Gao, Y. Shang, W. Zhu, W. Zhao, Z. Chen, H. Gong, Y. Yang, *Adv. Mater.* **2024**, *36*, 2305453.
[31] X. Zhang, Y. Yang, Y. Liu, Z. Jia, Q. Wang, L. Sun, L. C. Zhang, J. J. Kruzic, J. Lu, B. Shen, *Adv. Mater.* **2023**, *35*, 2303439.
[32] J. Fu, J. Ma, *Adv. Eng. Mater.* **2022**, *12*, 2200659.
[33] J. Johny, Y. Li, M. Kamp, O. Prymak, S. X. Liang, T. Krekeler, M. Ritter, L. Kienle, C. Rehbock, S. Barcikowski, S. Reichenberger, *Nano Res.* **2022**, *15*, 4807.
[34] Z. Zhang, Y. Liu, X. Su, Z. Zhao, Z. Mo, C. Wang, Y. Zhao, Y. Chen, S. Gao, *Nano Res.* **2022**, *16*, 6632.
[35] Y. Shi, M. Hou, J. Li, L. Li, Z. Zhang, *Acta Phys.-Chim. Sin.* **2022**, *38*, 2206020.
[36] Q. Ma, J. Young, S. Basuray, G. Cheng, J. Gao, N. Yao, W. Zhang, *Nano Today* **2022**, *45*, 101538.
[37] Z. H. Xue, H. C. Shen, P. Chen, G. X. Pan, W. W. Zhang, W. M. Zhang, S. N. Zhang, X. H. Li, C. T. Yavuz, *ACS Energy Lett.* **2023**, *8*, 3843.
[38] P. Gao, Z. Xue, S. Zhang, D. Xu, G. Zhai, Q. Li, J. Chen, X. Li, *Angew. Chem., Int. Ed.* **2021**, *60*, 20711.
[39] C. Wang, Z. Liu, T. Hu, J. Li, L. Dong, F. Du, C. Li, C. Guo, *ChemSusChem* **2021**, *14*, 1825.
[40] J. Yan, P. Liu, J. Li, H. Huang, W. Song, *Chem. Eng. J.* **2023**, *459*, 141601.
[41] M. A. Mushtaq, A. Kumar, W. Liu, Q. Ji, Y. Deng, G. Yasin, A. Saad, W. Raza, J. Zhao, S. Ajmal, Y. Wu, M. Ahmad, N. U. R. Lashari, Y. Wang, T. Li, S. Sun, D. Zheng, Y. Luo, X. Cai, X. Sun, *Adv. Mater.* **2024**, *36*, 2313086.
[42] L. Ouyang, J. Liang, Y. Luo, D. Zheng, S. Sun, Q. Liu, M. S. Hamdy, X. Sun, B. Ying, *Chin. J. Catal.* **2023**, *50*, 6.
[43] Y. Huang, C. He, C. Cheng, S. Han, M. He, Y. Wang, N. Meng, B. Zhang, Q. Lu, Y. Yu, *Nat. Commun.* **2023**, *14*, 7368.
[44] Q. Hu, K. Yang, O. Peng, M. Li, L. Ma, S. Huang, Y. Du, Z. X. Xu, Q. Wang, Z. Chen, M. Yang, K. P. Loh, *J. Am. Chem. Soc.* **2023**, *146*, 668.
[45] Q. Hu, S. Qi, Q. Huo, Y. Zhao, J. Sun, X. Chen, M. Lv, W. Zhou, C. Feng, X. Chai, H. Yang, C. He, *J. Am. Chem. Soc.* **2024**, *146*, 2967.
[46] Y. Liu, X. Zhang, Z. Chen, X. Zhang, P. Tsiakaras, P. K. Shen, *Appl Catal B* **2021**, *283*, 119606.

© 2024 Wiley-VCH GmbH

16163028, 0, Downloaded from https://onlinelibrary.wiley.com/doi/10.1002/adfm.202411325 by Shanxi University, Wiley Online Library on [07/10/2024]. See the Terms and Conditions (https://onlinelibrary.wiley.com/terms-and-conditions) on Wiley Online Library for rules of use; OA articles are governed by the applicable Creative Commons License